ACS Partner Journal

CHEMICAL & BIOMEDICAL IMAGING

Open Access

pubs.acs.org/ChemBioImaging

Article

Quantitative Assessment of Brain Glucose Metabolism Using Dynamic Glucose-Enhanced Magnetic Resonance Fingerprinting (DGE-MRF)

Mou Jiang, Yaping Yuan, Yue Zhu, Zhihao Zhou, Tian Xia, Louis-S. Bouchard, Shizhen Chen,* and Xin Zhou*

Cite This: https://doi.org/10.1021/cbmi.5c00213

Read Online

ABSTRACT: The brain relies heavily on glucose to sustain neuronal and glial functions, with metabolism closely regulated by both glucose levels and underlying physiological or pathological states. To investigate this complex process, a dynamic glucose-enhanced magnetic resonance fingerprinting (DGE-MRF) approach was implemented at a 9.4 T MRI system, integrating established multiparametric MRF with DGE-MRI and γ-variate kinetic modeling to track glucose uptake and clearance in gliomas. Dynamic ΔR_1, ΔR_2, and $\Delta R_{1\rho}$ curves revealed distinct temporal profiles: ΔR_1 peaked early, reflecting vascular glucose accumulation, whereas ΔR_2 and $\Delta R_{1\rho}$ captured slower tissue-level processes. Kinetic modeling using a γ-variate function demonstrated elevated glucose uptake rates (μ_{in}) and greater peak glucose changes (ΔG_{max}) in gliomas, while clearance rates (μ_{out}) were comparable to those of controls. Overall, DGE-MRF provides accurate, reproducible, and region-specific mapping of cerebral glucose kinetics, offering a noninvasive framework for probing metabolic heterogeneity in gliomas and potential applications in tumor characterization and neurodegenerative disease research.

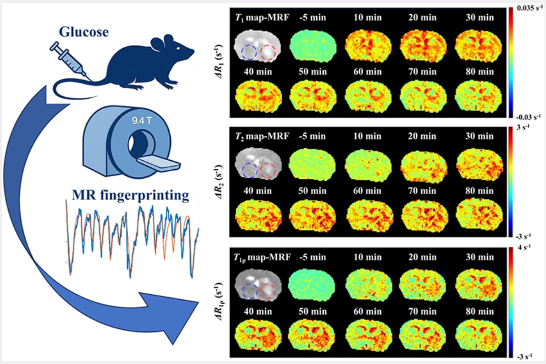

KEYWORDS: *magnetic resonance fingerprinting, dynamic glucose-enhanced, glioma, glucose metabolism, multiparametric mapping, kinetic modeling*

■ INTRODUCTION

The brain is the body's most energy-demanding organ, consuming about 20% of total energy, largely through glucose metabolism. Glucose supplies ATP to fuel neuronal and glial activity and supports neurotransmitter synthesis and other critical biochemical processes.[1] Furthermore, glucose metabolism is critical for neurotransmitter synthesis, generating vital metabolic intermediates and precursor molecules that influence brain function and neural signal transmission. Therefore, efficient glucose metabolism is fundamental to sustaining normal brain activity. Abnormalities in glucose metabolism can contribute to the development of various diseases, including gliomas, which rely on enhanced glycolysis and altered cellular environments for growth and survival.[2]

Quantitative kinetic modeling is essential for understanding and measuring glucose metabolism. The process can be described as follows: glucose from the bloodstream crosses the blood-brain barrier (BBB), enters cells via glucose transporters (GLUT), and is metabolized to produce ATP and other molecules. A simple γ-variate model provides a useful framework for approximating glucose metabolism.[3,4] The process can be characterized by two key parameters: the glucose uptake rate (μ_{in}) and the initial clearance rate (μ_{out}). These metabolic parameters are altered in regions with abnormal glucose metabolism, such as tumors. To support their rapid proliferation and high metabolic demands, tumor cells increase the expression of multiple glucose transporters, resulting in enhanced glucose uptake.[2] This is expected to be reflected by an increase in μ_{in}, while μ_{out} may also be modulated by the increased metabolic activity of tumors.

Current approaches for assessing glucose metabolism include positron emission tomography (PET) and magnetic resonance spectroscopy (MRS). ^{18}F-FDG PET remains the clinical gold standard, enabling highly sensitive and specific metabolic mapping. It is widely used in diagnosing tumors and neurodegenerative diseases, as well as in clinical research.[5] However, its reliance on radioactive tracers limits its use in

Received: October 29, 2025
Revised: December 7, 2025
Accepted: December 16, 2025

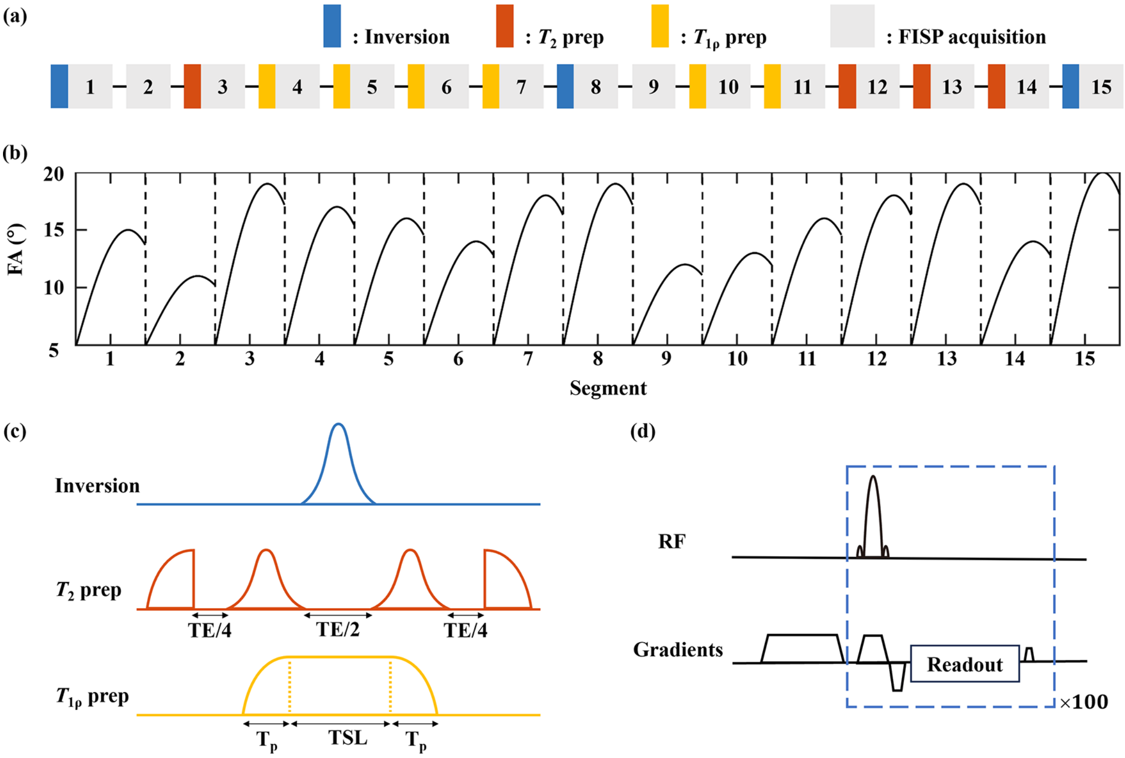

Figure 1. Pulse sequence design. (a) Schematic of the MRF sequence. (b) Flip-angle pattern. (c) Adiabatic preparation module. (d) FISP readout pattern.

vulnerable populations and restricts longitudinal studies. MRS provides a noninvasive alternative by detecting metabolic intermediates related to glycolysis in the healthy brain.[6,7] However, the relatively low sensitivity and spatial resolution restrict the precise localization of metabolic changes. More recent MRI-based approaches, such as chemical exchange saturation transfer (CEST) and chemical exchange spin-lock (CESL), detect metabolite changes indirectly through chemical exchange effects.[8,9] These techniques have shown promise for noninvasive glucose imaging, but each is sensitive to distinct physiological processes and therefore provides complementary information.[10,11]

Magnetic resonance fingerprinting (MRF) provides a novel framework for multiparametric quantitative imaging.[12] Unlike conventional weighted imaging, which provides only semi-quantitative contrast and requires separate scans for each parameter, MRF estimates several relaxation times from one acquisition and thus avoids registration errors between image sets. By varying acquisition parameters and employing dictionary-based signal matching, the MRF enables the simultaneous quantification of T_1, T_2, and other parameters within a single rapid scan. This technique enhances imaging efficiency, reproducibility, and tissue characterization compared with conventional MRI approaches.[13] Existing preclinical two-dimensional (2D) MRF sequences have been applied to dynamically quantify the transport of gadolinium-based contrast agents in tumor-bearing mouse models.[14] However, multiparametric MRF has not previously been combined with dynamic glucose-enhanced MRI and kinetic modeling to study the glucose metabolism in glioma. Establishing such an approach would offer a noninvasive platform for characterizing metabolic heterogeneity in gliomas. In this work, we focus on three relaxation parameters: T_1 (longitudinal relaxation time), T_2 (transverse relaxation time), and $T_{1\rho}$ (spin−lattice relaxation time in the rotating frame), with $T_{1\rho}$ being particularly sensitive to slow molecular motion and chemical exchange. Building on the original MRF framework, several groups have extended the method to simultaneous mapping of T_1, T_2, and $T_{1\rho}$ in phantoms and *in vivo*, demonstrating robust agreement with conventional relaxometry and good repeatability.[15−18]

Building on these developments, we adapted a two-dimensional FISP-based MRF sequence for simultaneous T_1, T_2, and $T_{1\rho}$ mapping during dynamic glucose-enhanced imaging at 9.4 T MRI in glioma-bearing brains. The sequence uses adiabatic preparation modules for T_1, T_2, and $T_{1\rho}$ to generate distinct contrast weightings, enabling multiparametric maps to be obtained in a single acquisition with an effective temporal resolution of 40 s. Although this temporal resolution is lower than that of single-parameter $T_{1\rho}$-weighted DGE protocols, it is sufficient to capture the relatively slow glucose kinetics of interest.[19] An iterative low-rank reconstruction was applied to recover high-quality T_1, T_2, and $T_{1\rho}$ maps from undersampled data. After validation in phantoms, the method was used *in vivo* to monitor glucose uptake and clearance across multiple brain regions following glucose administration. Finally, a γ-variate kinetic model was fitted to the dynamic data to quantify regional glucose transport, with particular emphasis on differences between glioma and contralateral healthy tissue.

■ METHODS

MRF Sequence Design

A DGE-MRF sequence was implemented by adapting a previously described two-dimensional FISP-based multiparametric MRF framework. The sequence generated T_1, T_2, and $T_{1\rho}$ maps within a 30.7 s acquisition, followed by a 9.3 s delay between repetitions, yielding an effective temporal resolution of 40 s. Each scan was divided into 15 acquisition segments with 100 images acquired per segment and a

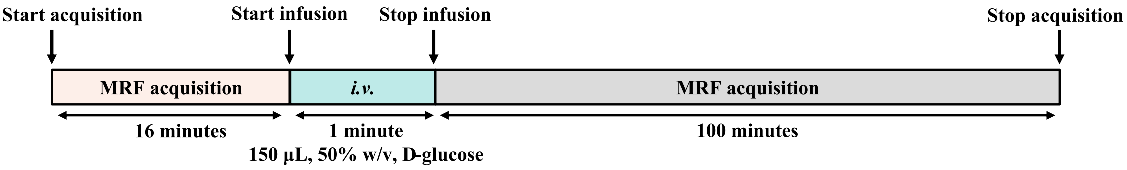

Figure 2. Experimental timeline. D-glucose (150 μL, 50% w/v) was injected intravenously at 150 μL/min.

dephasing gradient applied to produce an exact 2π phase dispersion across each voxel (Figure 1a,d).

To encode relaxation properties, each segment began with an adiabatic preparation module composed of three inversion recovery pulses (TI = 20, 100, 400 ms), four T_2-preparation pulses with two adiabatic refocusing pulses ($T_{2\text{pre}}$ = 30, 60, 40, 20 ms),[20] and six spin-lock preparations using adiabatic half-passage and reverse pulses at different spin-lock times (TSL = 20, 40, 60, 30, 15, 50 ms) with a spin-lock amplitude of 500 Hz (Figure 1c).[21] The use of adiabatic inversion, refocusing, and spin-lock pulses minimized B_1 inhomogeneity effects, ensuring uniform magnetization preparation across the imaging volume, particularly at 9.4 T. This combination of preparation modules generated distinct signal evolutions across multiple relaxation pathways, enabling simultaneous quantification of T_1, T_2, and $T_{1\rho}$ relaxation times from a single MRF acquisition. A spoiler gradient along the Z-axis followed each preparation to eliminate residual transverse magnetization.[22]

Following the preparation modules, a FISP acquisition module was applied using low flip angles (5° to 20°) to minimize B_1 sensitivity (Figure 1b). Excitations used 1 ms sinc pulses with 5 lobes. Data were acquired with a nonuniform spiral trajectory undersampled by a factor of 24.[23] The trajectory fully sampled k-space with 24 spiral interleaves separated by 15° rotations between adjacent arms, each acquiring 938 data points within a 4.7 ms readout. A 610 ms recovery delay was included to enhance T_1 sensitivity.[24] An additional 9.3 s delay was introduced between MRF repetitions in this initial DGE-MRF implementation to limit the overall gradient duty cycle and allow for complete magnetization recovery before the next repetition. Additional MRF imaging acquisition parameters were: TR/TE = 11.5 ms/1.1 ms, field of view = 25 × 25 mm^2, matrix = 128 × 128, and slice thickness = 1 mm. Compared with earlier T_1, T_2, and $T_{1\rho}$ MRF studies, this work introduces an adiabatic $T_{1\rho}$ preparation optimized for a 9.4 T preclinical system and applies it to the dynamic MRF monitoring of glucose uptake and clearance kinetics.

Dictionary Simulation

Signal dictionaries were generated by solving the Bloch equations by using the acquisition parameters described above. To account for dephasing in FISP readouts, each fingerprint was modeled as the vector sum of 81 isochromats with phase increments evenly distributed over 2π.[25] For the phantom study, the dictionary included 463,736 unique parameter combinations. T_1 values ranged from 300 to 1400 ms in steps of 20 ms. T_2 values ranged from 10 to 100 ms in steps of 1 ms. $T_{1\rho}$ values ranged from 10 to 100 ms in steps of 1 ms. For the *in vivo* study, approximately 1.94 million entries were simulated with finer sampling. T_1 values ranged from 1000 to 3000 ms with variable step sizes, while T_2 and $T_{1\rho}$ values ranged from 20 to 200 ms with progressively coarser steps at higher values.

Image Reconstruction

Undersampled data were reconstructed by using a low-rank subspace method. A temporal basis set was first estimated from the MRF dictionary using singular value decomposition (SVD), and the acquired data were then projected into this subspace. By calculating the coefficient maps after projection, high-quality time series images can be reconstructed. The reconstruction problem was formulated as[26−28]

$$\min_{\boldsymbol{c}} \|\boldsymbol{PFS\Phi c} - \mathbf{y}\|_2^2 + \lambda\,\|\boldsymbol{c}\|_* \qquad (1)$$

where $\boldsymbol{P}$, $\boldsymbol{F}$, $\boldsymbol{S}$, $\boldsymbol{\Phi}$, $\boldsymbol{c}$, and λ denote the undersampling pattern, nonuniform fast Fourier transform operator, coil sensitivity maps, temporal bases, coefficient maps, and regularization parameter, respectively. To ensure the retention of over 99% of the energy represented by the singular values, the first ten temporal principal components were selected as temporal bases ($\boldsymbol{\Phi}_{1-10}$). The corresponding coefficient maps ($\boldsymbol{c}_{1-10}$) were estimated and subsequently used to reconstruct the T_1, T_2, and $T_{1\rho}$ maps. Coil sensitivity maps ($\boldsymbol{S}$) were estimated using the ESPIRiT method, and the Fast Iterative Shrinkage-Thresholding Algorithm (FISTA) and conjugate gradient (CG) were employed to iteratively solve the optimization problem.[29,30]

Phantom Study

Phantoms containing 20 mM glucose with varying $MnCl_2$ concentrations (0.04 to 0. 3 mM) were scanned on a 9.4 T Bruker Biospec system. To validate the accuracy of the DGE-MRF method, the MRF sequence was compared with conventional methods: inversion recovery spin−echo for T_1, multiecho spin−echo for T_2, and spin-lock prepared spin−echo for $T_{1\rho}$. For T_1 mapping, acquisition parameters were TR = [50, 100, 300, 500, 1000, 2000, 5000, 10000] ms, TE = 6 ms, and scan time = 20.2 min. For T_2 mapping, the parameters were TR = 10000 ms, TE = [10, 20, 30,⋯, 200] ms, and scan time = 16.3 min. For $T_{1\rho}$ mapping, acquisition parameters were TR/TE = 10000 ms/5.12 ms and TSL = [5, 10, 20, 40, 60, 80, 120, 200] ms, scan time = 14.7 min. The spatial resolution used in the phantom study was identical to that used in the MRF sequence. To assess reproducibility, repeated measurements were performed on the same phantom at different time points.

In Vivo Study

All animal procedures were performed in compliance with the Institutional Animal Care and Use Committee guidelines of the Innovation Academy for Precision Measurement Science and Technology. GL-261 glioma cells (1 × 10^8 cells/mL, 10 μL) were injected into the right thalamus of six female C57BL/6 mice (7 weeks old, 20.0 ± 1.2 g). Imaging was performed 11−14 days post-implantation. Mice were allowed access to water on the day of the experiment and did not fast overnight.

During experiments, mice were anesthetized with isoflurane (2−3% induction, 1−1.5% maintenance). Baseline data were acquired with a 16 min continuous MRF scan. Next, 150 μL of a 50% w/v glucose solution was injected intravenously (150 μL/min), followed by continuous MRF imaging for 100 min (Figure 2). Body temperature was maintained at 37.0 ± 0.2 °C using a heater.

Relaxation maps (T_1, T_2, and $T_{1\rho}$) from each time point were converted to relaxation rates using the relationships $R_1 = 1/T_1$, $R_2 = 1/T_2$, and $R_{1\rho} = 1/T_{1\rho}$. Data acquired during the 16 min period before glucose injection were averaged to establish a baseline. Dynamic changes were then calculated as ΔR_1, ΔR_2, and $\Delta R_{1\rho}$ relative to preinjection baseline values. These changes were used as surrogate measures of the glucose concentration dynamics in brain tissue.

To assess whether DGE-MRF signal changes reflected glucose-specific metabolic processes rather than nonspecific effects, we performed a metabolic blockade experiment in 12 healthy female C57BL/6 mice (10 weeks old, 25 ± 1.4 g). Animals were randomly assigned to a 2DG group (n = 6) or a control group (n = 6). Mice in the 2DG group received the glucose uptake inhibitor 2-deoxy-D-glucose (2DG; 20% w/v, 0.8 g/kg, tail-vein injection) 2 h before the DGE-MRF scan, whereas control mice underwent the same imaging protocol without 2DG pretreatment. Two hours after 2DG or control handling, glucose was administered, and DGE-MRF data were acquired as described above.

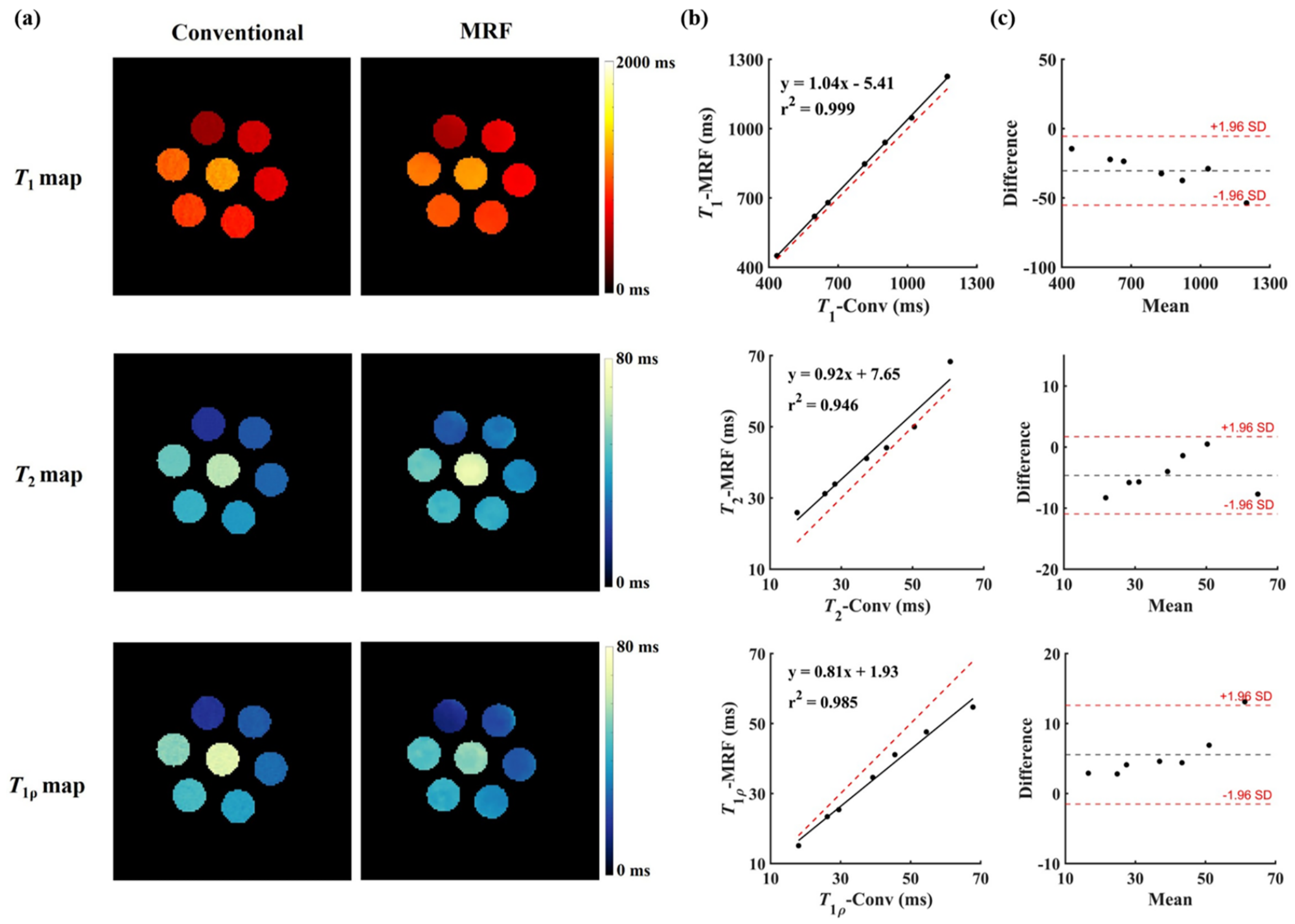

Figure 3. Validation in phantoms. (a) T_1, T_2, and $T_{1\rho}$ maps from conventional methods and the MRF sequence. (b) Mean relaxation times with the dashed red line indicating the line of identity ($y = x$). (c) Bland−Altman plots comparing the two methods. Black dashed lines show mean bias, and red dashed lines indicate limits of agreement (±1.96 SD).

Kinetic Modeling

Glucose uptake in the brain is governed by concentration gradients between blood and tissue and is mediated by glucose transporters. Once transported into cells, glucose is phosphorylated by hexokinase to form glucose-6-phosphate. The enzymatic activity of hexokinase is feedback-regulated by glucose-6-phosphate levels, with high concentrations inhibiting hexokinase and slowing metabolism, whereas low concentrations relieve inhibition and enhance glucose utilization. To describe glucose uptake and clearance dynamics, a γ-variate function was employed:[3,4]

$$\Delta \text{Glu}_{\text{brain}}(t) = A\cdot(t - t_0)^{1/\mu_{\text{in}}}\cdot \text{e}^{-\mu_{\text{out}}(t-t_0)} \tag{2}$$

where $\Delta\text{Glu}_{\text{brain}}$ is the glucose concentration change in the brain (mM), μ_{in} and μ_{out} are uptake and clearance rates (min^{-1}), and A is the amplitude constant. The γ-variate function has been widely used in dynamic susceptibility contrast MRI as a compact representation of bolus-tracking curves, as it captures the asymmetric rise and fall of concentration−time profiles with few parameters.[3] In the context of DGE-MRF, this form provides a physiologically motivated yet simple description of the glucose response, allowing uptake and clearance behavior to be characterized without the additional complexity of full multicompartment kinetic models.

Because glucose molecules contain five exchangeable hydroxyl protons that rapidly exchange with bulk water protons, variations in the glucose concentration induce measurable changes in T_2 and $T_{1\rho}$. The magnitude of these changes is linearly proportional to glucose concentration. In this study, $\Delta R_{1\rho}$ was used to estimate $\Delta\text{Glu}_{\text{brain}}$ according to the following equation:[11]

$$\Delta \text{Glu}_{\text{brain}} = \frac{\Delta R_{1\rho}}{r_{\text{g}}} \tag{3}$$

with r_{g} representing the glucose $R_{1\rho}$ relaxivity (s^{-1}·mM^{-1}). The peak glucose concentration change (ΔG_{max}, mM) was derived from these model fits.

Statistical Analysis

Agreement between MRF-derived and conventional relaxation measurements, as well as reproducibility between repeated scans, was evaluated using linear regression and Bland−Altman analysis. For the Bland−Altman method, differences between paired measurements were plotted against their means, with 95% limits of agreement indicated.

Parameters of the γ-variate model were estimated by using the MATLAB function lsqcurvefit. Regional differences in kinetic parameters across brain areas were analyzed with repeated-measures ANOVA, followed by Tukey's post hoc test to correct for multiple comparisons. Statistical significance was defined as $p < 0.05$ after adjustment. All image analysis and data processing were performed using custom MATLAB scripts (R2023b, MathWorks).

■ RESULTS

Phantom and *In Vivo* Validation

Phantom experiments showed that relaxation maps derived from the MRF sequence were consistent with those obtained by using conventional methods (Figure 3a). Under 24-fold

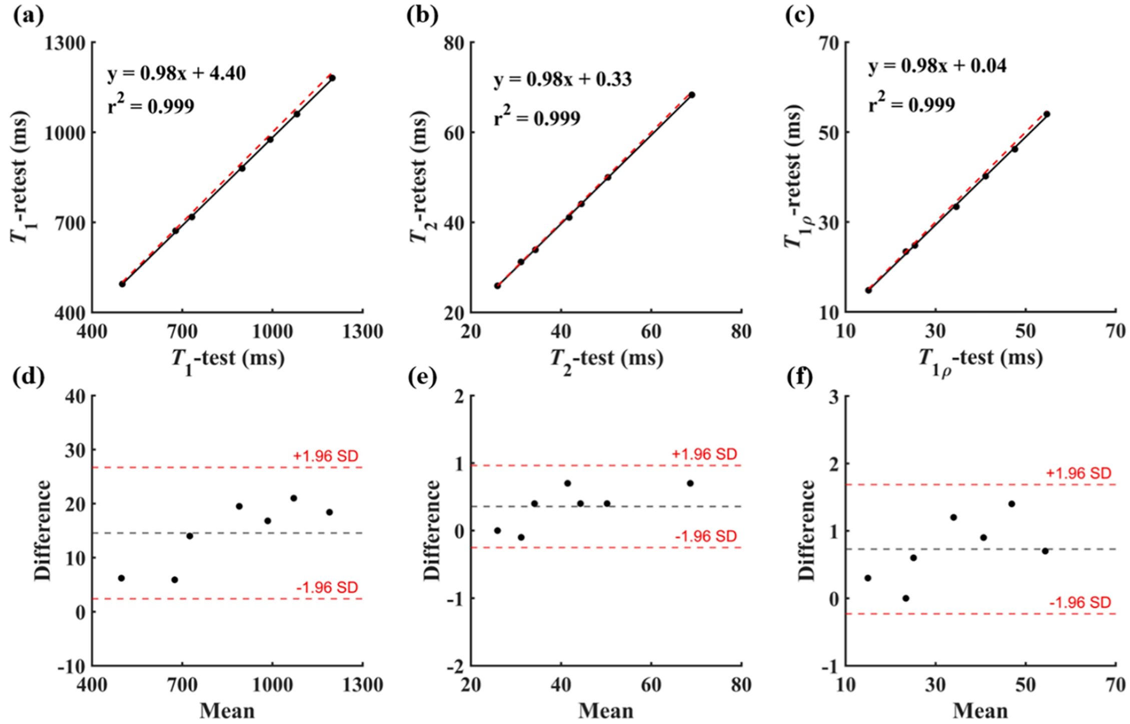

Figure 4. Repeatability assessment in phantoms. Regression plots (a−c) and Bland−Altman analyses (d−f) of repeated scans for T_1 (a, d), T_2 (b, e), and $T_{1\rho}$ (c, f).

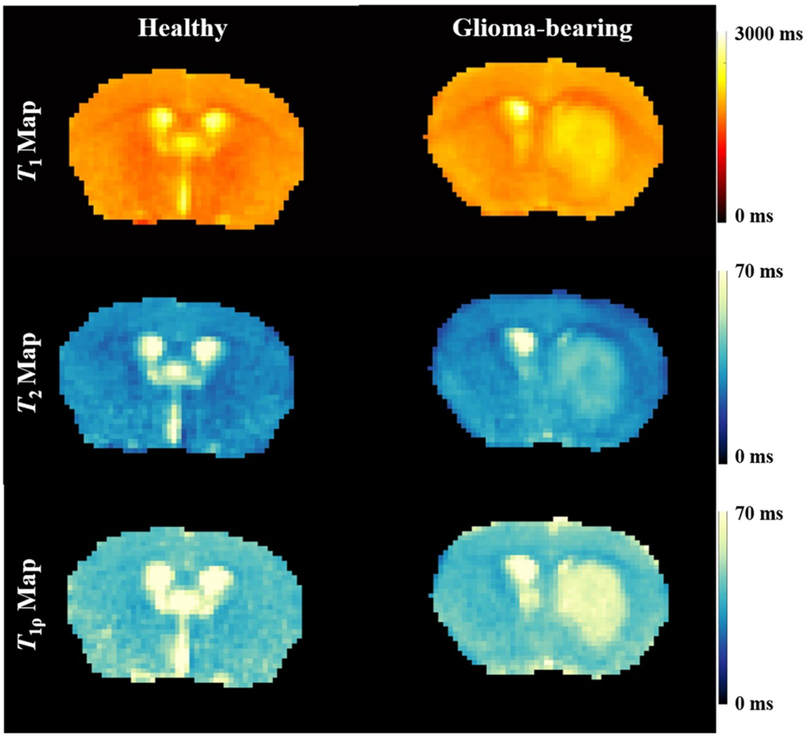

Figure 5. Representative T_1, T_2, and $T_{1\rho}$ maps from a healthy mouse brain (left column) and a glioma-bearing mouse brain (right column) acquired with the proposed DGE-MRF sequence.

undersampling, relaxation times correlated closely with reference values, with r^2 exceeding 0.94 for all parameters (Figure 3b). T_1 values showed high correlation (r^2 = 0.999), while T_2 and $T_{1\rho}$ were slightly underestimated but still well correlated (r^2 = 0.946 and 0.985, respectively). Bland−Altman analyses indicated narrow 95% limits of agreement centered near zero, suggesting a limited systematic bias (Figure 3c).

Reproducibility was evaluated through repeated phantom scans (Figure 4). Test−retest correlations remained high (r^2 = 0.999), and Bland−Altman plots showed small mean differ-

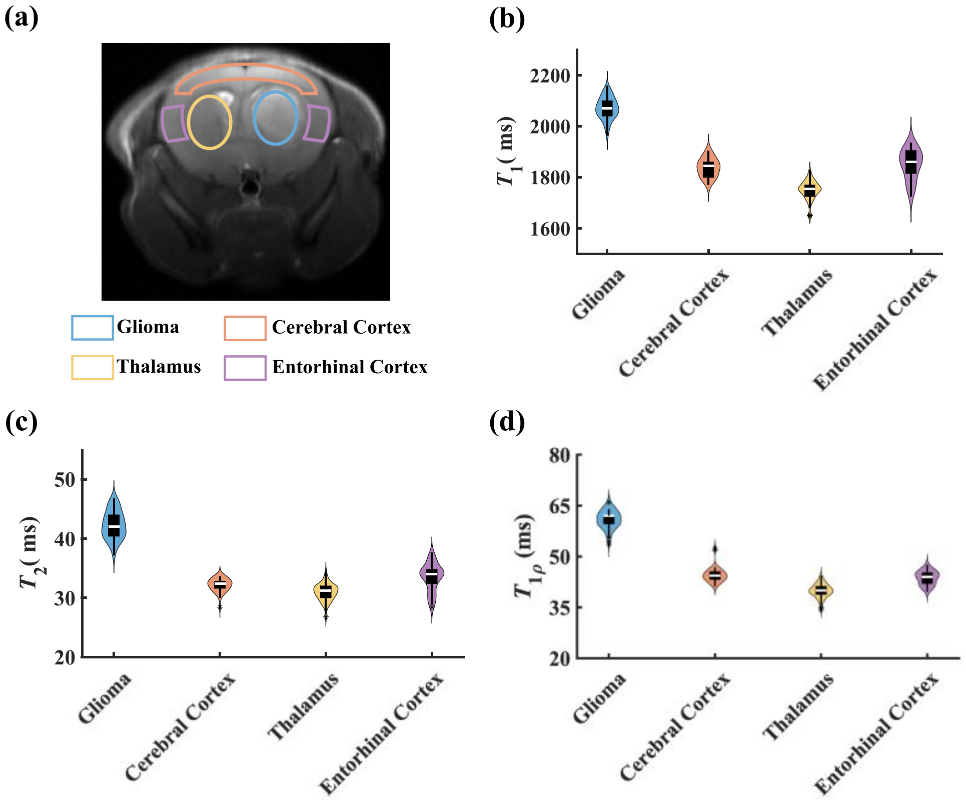

Figure 6. Regional relaxation times in glioma-bearing mouse brain. (a) Representative anatomical image showing regions of interest (ROIs) drawn in glioma, cerebral cortex, thalamus, and entorhinal cortex. (b−d) Violin plots of quantitative T_1, T_2, and $T_{1\rho}$ values, respectively, in these ROIs.

ences between scans (14.54 ms for T_1, 0.36 ms for T_2, and 0.73 ms for $T_{1\rho}$), confirming stable measurement repeatability.

T_1, T_2, and $T_{1\rho}$ maps were obtained in both healthy and glioma-bearing mouse brains under 24-fold undersampling (Figure 5). The major anatomical structures were clearly delineated across all three relaxation maps. However, in cerebrospinal fluid (CSF) regions, T_2 and $T_{1\rho}$ values were slightly underestimated due to CSF flow and diffusion effects associated with the dephasing gradient. Glioma regions consistently exhibited elevated relaxation times compared to the surrounding healthy tissue. Quantitative analysis across four brain regions confirmed this pattern, with gliomas showing the highest relaxation values (T_1: 2071.21 ± 42.33 ms; T_2: 42.29 ± 2.31 ms; $T_{1\rho}$: 60.94 ± 2.66 ms). In contrast, the contralateral thalamus demonstrated values (T_1: 1749.16 ± 38.02 ms; T_2: 30.94 ± 1.43 ms; $T_{1\rho}$: 39.97 ± 2.06 ms) comparable to those of other nontumor regions (Figure 6).

Dynamic Mapping of Glucose Transport

Continuous monitoring of ΔR_1, ΔR_2, and $\Delta R_{1\rho}$ after glucose administration is shown in Figure 7. All three parameters displayed the expected rise-and-fall pattern of the glucose metabolism. The temporal evolution of ΔR_1 differed from that of ΔR_2 and $\Delta R_{1\rho}$. ΔR_1 rose rapidly across the brain, peaking at ~20 min, with no initial difference between glioma and healthy tissue. Thereafter, ΔR_1 declined in healthy regions but remained plateaued in gliomas (Figure 7a,b). The mean ΔR_1 curves for glioma and contralateral thalamus intersected at around 40 min, indicating that ΔR_1 alone does not provide stable tumor−normal separation over the full time course. After this crossover, the ΔR_1 maps acquired beyond 40 min (Figure 7a) show progressively increased contrast between the tumor and surrounding healthy tissue.

In contrast, ΔR_2 and $\Delta R_{1\rho}$ exhibited slower dynamics, with elevated signals emerging first in gliomas and declining gradually over time (Figure 7c,e). Averaged curves across six mice confirmed this pattern: both ΔR_2 and $\Delta R_{1\rho}$ changes were larger in glioma than in contralateral thalamus, with peak times delayed relative to ΔR_1 (35 min vs 20 min; Figure 7d,f).

Figure 7b,d,f presents the DGE dynamic curves from regions of interest (ROIs) in tumor and contralateral healthy brain tissue across six mice. Despite individual variability, all mice exhibited a consistent trend of an initial increase followed by a gradual decline. Among the three parameters, $\Delta R_{1\rho}$ displayed the lowest intersubject variance, indicating greater stability and reliability in reflecting the glucose concentration changes in brain tissue.

Kinetic Modeling of Glucose Metabolism

Glucose uptake dynamics were quantified by fitting $\Delta R_{1\rho}$ curves with a γ-variate model (eqs 2 and 3). The model provided robust fits across brain regions, accurately reproducing both peak responses and subsequent decay. Regional analysis revealed clear metabolic heterogeneity (Figure 8 and Table 1). Glioma tissue showed significantly higher uptake rates (μ_{in}: 1.71 ± 0.30 vs 0.93 ± 0.16 min^{-1}, $p = 0.009$) and greater peak glucose change ($\Delta G_{\max}$: 31.87 ± 2.69 vs 21.25 ± 2.55 mM, $p = 0.001$) compared with controls. Clearance rates were lower in gliomas (μ_{out}: 0.018 ± 0.003 vs 0.028 ± 0.008 min^{-1}, $p = 0.019$). Beyond tumor−control differences, variations were also observed among healthy regions, underscoring the sensitivity of DGE-MRF-based kinetic modeling in detecting spatially heterogeneous metabolic activity.

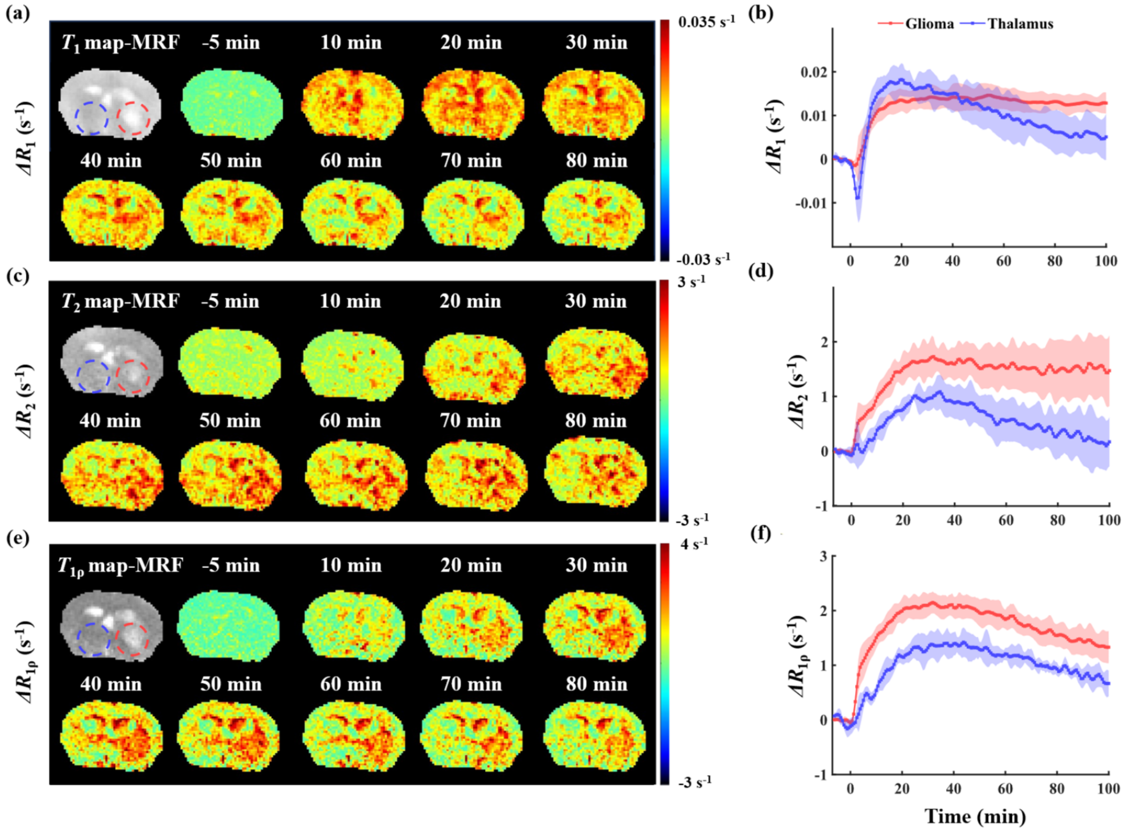

Figure 7. Dynamic changes in ΔR_1, ΔR_2, and $\Delta R_{1\rho}$ after glucose injection in glioma-bearing mouse brains. (a, c, e) Brain tissue contrast images of a representative glioma-bearing mouse. (b, d, f) Averaged ΔR_1, ΔR_2, and $\Delta R_{1\rho}$ values (mean ± SD, $n = 6$) in glioma tissue and contralateral normal brain tissue.

2DG Blockade Validates Glucose Specificity

In the 2DG blockade experiment, group-averaged ΔR_1, ΔR_2, and $\Delta R_{1\rho}$ time courses with and without 2DG pretreatment are shown in Figure 9. Following glucose injection, both groups exhibited a rapid increase in ΔR_1, but their subsequent behavior diverged. In the control group, ΔR_1 gradually declined toward baseline, whereas in the 2DG-pretreated group, the decay was substantially slower (Figure 9a). For ΔR_2 and $\Delta R_{1\rho}$, the control group displayed a typical rise-and-fall pattern, with a clear peak followed by gradual recovery toward the baseline (Figure 9b,c). In contrast, in the 2DG-pretreated group, both ΔR_2 and $\Delta R_{1\rho}$ continued to increase over the entire 100 min observation window and showed no obvious clearance. The initial slope of the $\Delta R_{1\rho}$ response was also lower with 2DG, indicating a reduced apparent uptake rate. Consistent with these observations, γ-variate fitting revealed reduced effective uptake and clearance rates in the 2DG-pretreated group compared with controls (2DG vs without 2DG: μ_{in}, 0.83 ± 0.12 vs 1.10 ± 0.11 min^{-1}, $p = 0.002$; μ_{out}, 0.014 ± 0.003 vs 0.0296 ± 0.006 min^{-1}, $p = 0.001$). Together, these findings support partial inhibition of glucose transport and metabolism by 2DG and reinforce that the DGE-MRF signal predominantly reflects glucose-dependent metabolic processes rather than nonspecific osmotic or hemodynamic effects.

■ DISCUSSION

In this study, we combined dynamic glucose-enhanced MRI with multiparametric magnetic resonance fingerprinting (DGE-MRF) at 9.4 T to obtain simultaneous T_1, T_2, and $T_{1\rho}$ maps, together with glucose kinetic parameters in glioma-bearing mouse brains. Validation experiments demonstrated close agreement between MRF-derived and conventional relaxation measurements, confirming the accuracy of the method. *In vivo* mapping further distinguished healthy from glioma-bearing mouse brains, revealing clear structural differences. The sequence design incorporated adiabatic preparation pulses to reduce B_1 inhomogeneity and a low-rank subspace reconstruction to suppress undersampling artifacts and enhance temporal SNR.[20,21,26] These choices enabled high-resolution 2D imaging (0.195 mm) within ~30 s, with voxel sizes nearly 30-fold smaller than those typically achievable in clinical studies. Although higher field strength improved the SNR, it did not fully compensate for the signal loss from reduced voxel size. This suggests that the method may also be well suited for lower field strengths (3 or 5 T), where larger voxels provide higher SNR. Compared with conventional DGE-MRI, this approach enhances quantitative accuracy by directly generating relaxation maps rather than relying on weighted image fitting, reducing errors associated with motion and signal quantification. The temporal resolution is longer than the ~7 s reported for single-parameter $T_{1\rho}$-weighted DGE, but, to our knowledge, this is the first demonstration of full multiparametric T_1, T_2, and $T_{1\rho}$ mapping during dynamic glucose infusion.[19] Collectively, these features position DGE-MRF as a practical and versatile framework for probing cerebral glucose metabolism.

Phantom validation experiments demonstrated that the proposed DGE-MRF method achieved good accuracy and reproducibility. However, slight discrepancies in relaxation

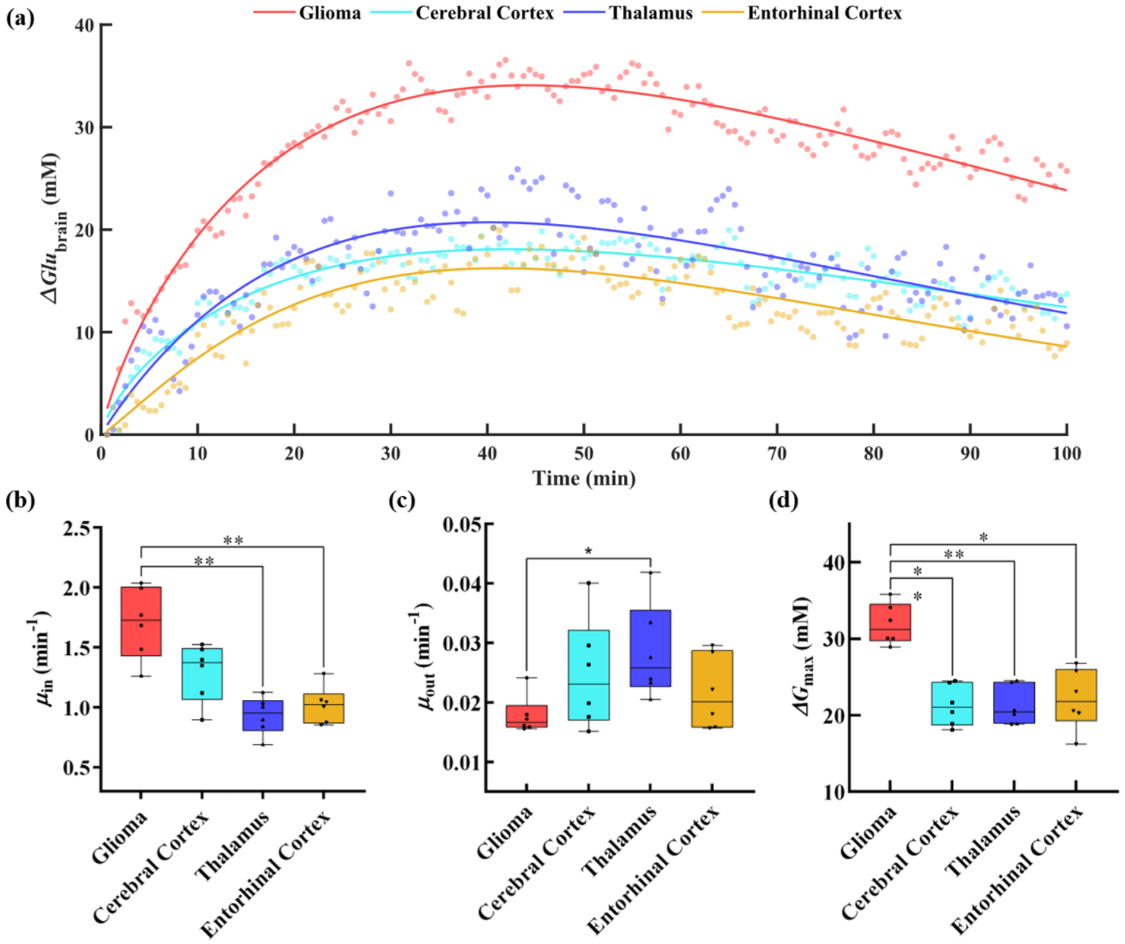

Figure 8. Kinetic modeling of cerebral glucose metabolism. (a) Fitted γ-variate curves for glioma, cerebral cortex, thalamus, and entorhinal cortex. (b−d) Comparison of fitted μ_{in}, μ_{out}, and ΔG_{max} parameters across brain regions in six mice. Significance levels: $*p < 0.05$ and $**p < 0.01$.

Table 1. Estimates of the Mean (± SD) for Kinetic Parameters in Different Brain Tissues of Glioma-Bearing Mice

	glioma	cerebral cortex	thalamus	entorhinal cortex
μ_{in} (min^{-1})	1.71 ± 0.30	1.29 ± 0.24	0.93 ± 0.16	1.02 ± 0.16
μ_{out} (min^{-1})	0.018 ± 0.003	0.025 ± 0.009	0.028 ± 0.008	0.022 ± 0.006
ΔG_{max} (mM)	31.87 ± 2.69	21.30 ± 2.69	21.25 ± 2.55	22.12 ± 3.91

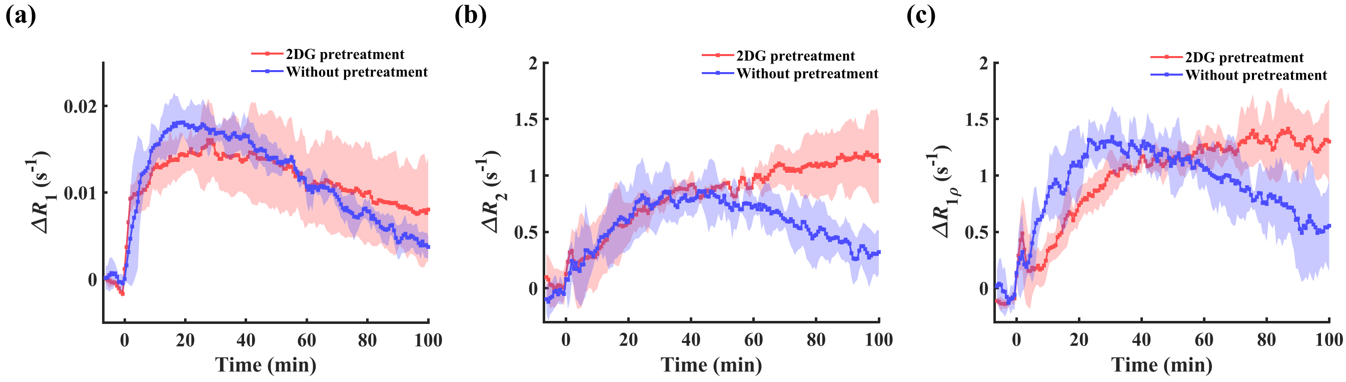

Figure 9. Effect of the 2DG pretreatment on DGE-MRF relaxation changes. Group-averaged time courses of (a) ΔR_1, (b) ΔR_2, and (c) $\Delta R_{1\rho}$ in mouse brains after glucose injection were calculated by comparing the 2DG-pretreated group with the untreated control group.

times were observed compared with those of standard reference sequences. This difference primarily arises from the sensitivity of the dephasing gradient used in the readout module to diffusion effects. When diffusion is not considered, the use of stronger dephasing gradients in FISP-based MRF can lead to underestimation of T_2 values, particularly in tissues such as CSF that exhibit high T_2 and apparent diffusion coefficients (ADC).[31] As a result, T_1, T_2, and $T_{1\rho}$ values obtained with DGE-MRF may differ slightly from those measured by conventional methods. To balance off-resonance artifact suppression and diffusion sensitivity, a dephasing gradient of 2π was employed in this study. In future work, diffusion effects will be explicitly incorporated into both the pulse sequence and the signal dictionary to further minimize gradient-induced relaxation bias.

In vivo, the proposed DGE-MRF technique enabled continuous monitoring of glucose dynamics across different brain regions, providing insights into both vascular- and tissue-level processes. After glucose administration, ΔR_1, ΔR_2, and $\Delta R_{1\rho}$ dynamics showed the expected rise and subsequent decline.[4,32] In glioma-bearing mice, relaxation changes varied across regions. ΔR_1 increased rapidly, peaking at 20 min, before gradually declining. This early rise likely reflects vascular glucose accumulation, which increases blood viscosity and reduces diffusivity, thereby enhancing ΔR_1.[33,34] The earlier ΔR_1 peak (20 min) compared with those of ΔR_2 and $\Delta R_{1\rho}$ (both 35 min) suggests that ΔR_1 is more sensitive to vascular glucose levels. By contrast, ΔR_2 and $\Delta R_{1\rho}$ are less affected by blood flow and better reflect tissue-level changes.[32] The decline in ΔR_1 reflects the progressive glucose clearance, which occurs more rapidly in healthy tissue than in gliomas. The slower clearance in tumors is likely driven by blood−brain barrier disruption and increased vascularization, leading to sustained glucose accumulation in both tumor tissue and nearby capillaries. Analysis of ΔR_2 and $\Delta R_{1\rho}$ further revealed that glioma regions had larger signal changes and higher uptake rates.[35] The differences in ΔR_2 may partly reflect microstructural effects: infiltration of tumor cells reduces white matter anisotropy, which otherwise contributes to dipolar interactions affecting R_2.[36] Spin-lock preparation, which minimizes dipolar angle dependence, makes $\Delta R_{1\rho}$ a more direct indicator of glucose concentration variation.[37]

To further quantify these dynamics, $\Delta R_{1\rho}$ curves were fitted with a γ-variate model, which captures both uptake and clearance kinetics. Analysis of the first 100 min of the DGE curves provided an initial assessment of vascular−tissue kinetics. Glioma regions exhibited higher μ_{in} and $\Delta G_{\max}$ than healthy tissue, consistent with the increased activity and abundance of glucose transporters in tumor vasculature and cell membranes. This metabolic adaptation reflects the imbalance between rapid cellular proliferation and limited vascular supply, which generates a hypoxic microenvironment. Under hypoxia, stabilization of hypoxia-inducible factor-1α (HIF-1α) upregulates GLUT1 and GLUT3 expression, thereby enhancing glucose uptake and sustaining glycolysis.[38,39]

Within the tumor microenvironment, accelerated glucose consumption represents a key metabolic adaptation that sustains growth. This pattern is consistent with the Warburg effect, whereby cancer cells preferentially rely on glycolysis even under aerobic conditions, resulting in markedly increased glucose utilization.[40] In our study, however, μ_{out} in tumors was not significantly higher than in healthy tissue, consistent with previous reports.[35] Two factors may explain this finding. First, elevated systemic glucose levels may limit the ability of the tissue to clear glucose efficiently.[4] Second, clearance partly depends on neuronal activity, which is reduced under anesthesia. Suppressed synaptic activity lowers GLUT-mediated transport and phosphorylation, thereby reducing cerebral glucose consumption and influencing the measurement of μ_{out}.[41]

From a metabolic imaging perspective, these findings indicate that $\Delta R_{1\rho}$ provides the most robust tumor−normal contrast among the three relaxation parameters, consistent with previous $T_{1\rho}$-weighted DGE and glucoCESL studies showing high sensitivity of $T_{1\rho}$ to glucose uptake in tumors.[11,19,42] However, T_1 and T_2 contribute complementary information. ΔR_1 is mainly driven by changes in vascular and extracellular glucose concentrations and therefore reflects blood−brain barrier integrity and perfusion, whereas ΔR_2 is influenced by microstructural changes and intracellular glucose levels. Joint analysis of ΔR_1, ΔR_2, and $\Delta R_{1\rho}$ can thus help separate vascular- from tissue-specific contributions to the DGE signal. In this context, our triparametric DGE-MRF implementation is best viewed as a platform for comprehensive metabolic characterization rather than as an attempt to optimize temporal resolution for $T_{1\rho}$-based tumor detection alone. The primary aim of this work is methodological: to establish and validate a DGE-MRF framework for multiparametric mapping of glucose kinetics *in vivo* using glioma as an illustrative application rather than the sole focus of detection.

From a modeling perspective, we chose a γ-variate function as a simple, yet physiologically grounded, representation of the DGE-MRF response. This function has been widely used in dynamic susceptibility contrast MRI to describe bolus-tracking curves, where the initial rise reflects tracer delivery and the subsequent decay reflects clearance and redistribution.[3] Here, we applied the same formulation to the $\Delta R_{1\rho}$ time course after glucose injection: the ascending phase is dominated by glucose delivery and accumulation in the vascular and extracellular spaces, whereas the descending phase reflects the combined effects of clearance from the circulation, transport across the blood−brain barrier, cellular uptake, and downstream metabolism.[35] In this context, μ_{in} and μ_{out} are best viewed as apparent, semiquantitative indices that summarize the overall response shape rather than absolute metabolic rates. Under the present experimental conditions, more detailed multicompartment kinetic models would require many additional, weakly constrained parameters and would therefore increase the risk of overfitting.

2DG is a glucose analogue that enters cells via GLUT transporters but cannot be fully metabolized. The presence of 2DG would reduce the effective rate of glucose uptake. Once inside the cell, 2DG is phosphorylated by hexokinase to 2DG-6-phosphate, which, unlike glucose-6-phosphate, does not proceed through glycolysis and therefore accumulates. The buildup of 2DG-6-phosphate feeds back to inhibit hexokinase, further limiting glucose phosphorylation and slowing overall glucose utilization and clearance.[43,44] Consistent with this mechanism, our 2DG blockade experiment indicates that the DGE-MRF signal predominantly reflects glucose-dependent metabolism rather than nonspecific changes in the osmolarity or blood flow. In the control group, ΔR_1, ΔR_2, and $\Delta R_{1\rho}$ all showed a transient increase after glucose administration, followed by a gradual return toward baseline. In contrast, 2DG pretreatment markedly altered these time courses: ΔR_1 still rose rapidly in both groups but decayed more slowly with 2DG, and ΔR_2 and $\Delta R_{1\rho}$ in the 2DG group continued to increase over the entire 100 min observation period without a clear return to baseline, indicating slower apparent glucose clearance. The initial $\Delta R_{1\rho}$ increase was also less steep after 2DG, consistent with a reduced apparent uptake rate. Together, these observations support partial inhibition of normal glucose metabolism by 2DG and reinforce that changes in ΔR_1, ΔR_2, and especially $\Delta R_{1\rho}$ primarily capture alterations in glucose transport and metabolism.

In particular, the reliability and physiological specificity of μ_{in} and μ_{out} are constrained by the lack of a directly measured arterial input function (AIF) for the injected glucose. In the absence of an explicit AIF, the γ-variate model is fitted directly to tissue $\Delta R_{1\rho}$ curves, so μ_{in}, μ_{out}, and $\Delta G_{\max}$ reflect the combined effects of the vascular input, transport across the blood−brain barrier, and tissue metabolism.[45] These parameters should therefore be viewed as apparent, semiquantitative indices rather than fully quantitative kinetic rate constants as in models that incorporate an independent AIF. In small-animal MRI, robust AIF estimation is challenging because of the small caliber of cerebral arteries, rapid bolus passage, and strong partial-volume effects, and the present DGE-MRF protocol was not optimized for high-temporal-resolution AIF measurement. Future work will seek to combine higher-temporal-resolution DGE-MRF acquisitions with dedicated AIF assessment, for example, by targeting major cerebral arteries or using independent blood sampling. This integration should enable more physiologically grounded compartmental modeling and improve the quantitative accuracy of DGE-MRF−derived kinetic parameters.[46]

^{18}F-FDG PET is widely regarded as the clinical reference standard for assessing glucose metabolism in brain tumors. In this preclinical study, however, ^{18}F-FDG PET was not acquired in the same cohort of glioma-bearing mice, so DGE-MRF−derived μ_{in} and $\Delta G_{\max}$ cannot be directly compared with the standardized uptake value (SUV).[47] Nevertheless, the elevated μ_{in} and $\Delta G_{\max}$ observed in gliomas relative to contralateral tissue mirror the well-established pattern of increased FDG uptake in high-grade tumors, where SUV−time curves show a steeper early rise and higher peak SUV in tumor regions than in normal brain. These parallels suggest that DGE-MRF provides information on tumor glucose handling comparable to FDG PET, while offering higher spatial resolution and multiparametric readouts without ionizing radiation. Future multimodal studies that combine DGE-MRF with ^{18}F-FDG PET in the same animals or in patients will be important to establish direct quantitative relationships between μ_{in} and FDG SUV.

The framework established here could be extended to investigate additional metabolic pathways beyond vascular−tissue glucose exchange, particularly the exchange between brain parenchyma and CSF.[4] Glucose dynamics within the CSF play an important role in maintaining neuronal energy homeostasis and reflect both the BBB and blood−CSF barrier function. Abnormal CSF glucose regulation has been associated with various neuropathological conditions, including neuroinflammation, metabolic disorders, and neurodegenerative diseases. However, the current 2D FISP-based MRF sequence is inherently sensitive to diffusion effects arising from CSF flow, which can introduce signal attenuation and bias in relaxation parameter estimation, thereby limiting the accuracy of DGE curve quantification in CSF regions.[31] Incorporating diffusion-weighted or flow-compensated modules into the MRF framework could help mitigate these confounding effects. Moreover, transitioning to an accelerated three-dimensional (3D) MRF acquisition would enable volumetric coverage of the entire brain and improve the ability to capture glucose transport across the blood, tissue, and CSF compartments simultaneously. Such an approach could offer a more integrated view of cerebral glucose metabolism, facilitating the exploration of interactions among vascular delivery, parenchymal uptake, and CSF clearance under both physiological and pathological conditions.

However, this study has several limitations. First, it was conducted in a relatively small cohort of glioma-bearing mice ($n = 6$) and was therefore underpowered to detect subtle effects or potential sex-related differences. Second, although anesthesia and general physiology were managed according to institutional small-animal MRI procedures, continuous invasive monitoring of the mean arterial pressure, blood gases, and blood glucose was not performed. Future work will address these issues by including larger, mixed-sex cohorts with power-based sample size estimation and by incorporating comprehensive physiological monitoring, thereby improving the robustness and generalizability of the DGE-MRF-derived metabolic parameters. Future optimization will focus on reducing the number of sampling modules and shortening the sequence length, while incorporating inter-repetition delay times into the magnetization evolution dictionary. Under the constraints of duty cycle and specific absorption rate (SAR), these adjustments could substantially enhance temporal resolution, improving sensitivity to rapid physiological processes such as AIF characterization. Moreover, such acceleration would free additional acquisition time for implementing 3D DGE-MRF with whole-brain coverage. Besides, temporal fluctuations observed in the relaxation maps suggest that further optimization of sequence design and reconstruction is needed. Physics-informed MRF optimization frameworks and accelerated 3D implementations could improve both measurement stability and temporal fidelity for future metabolic imaging studies.[48]

■ CONCLUSIONS

This study demonstrates that the DGE-MRF sequence enables accurate and reproducible mapping of T_1, T_2, and $T_{1\rho}$ relaxation times for the dynamic assessment of brain glucose metabolism. Phantom experiments confirmed method reliability, and *in vivo* studies revealed elevated relaxation values, faster uptake, and greater glucose accumulation in gliomas compared with healthy tissue, consistent with tumor-driven metabolic adaptations. By conversion of relaxation maps into ΔR_1, ΔR_2, and $\Delta R_{1\rho}$ dynamics and application of kinetic modeling, the approach provided quantitative insights into glucose uptake and clearance. Although this study was limited by the absence of arterial input functions and the sensitivity of 2D imaging to CSF flow, future advances in accelerated 3D MRF and optimized sequence design are expected to overcome these challenges, enabling whole-brain, high-resolution metabolic imaging. Beyond oncology, impaired glucose metabolism plays a central role in neurodegenerative disorders, and the proposed DGE-MRF framework offers a promising noninvasive tool for early detection, longitudinal monitoring, and therapeutic evaluation across a broad range of neurological diseases.

■ ASSOCIATED CONTENT

Data Availability Statement

The experimental data, images, and code from this study are available upon request to the corresponding author.

AUTHOR INFORMATION

Corresponding Authors

Shizhen Chen − *State Key Laboratory of Magnetic Resonance Spectroscopy and Imaging, National Center for Magnetic Resonance in Wuhan, Wuhan Institute of Physics and Mathematics, Innovation Academy for Precision Measurement Science and Technology, Chinese Academy of Sciences-Wuhan National Laboratory for Optoelectronics, Huazhong University of Science and Technology, Wuhan 430071, P. R. China; University of Chinese Academy of Sciences, Beijing 100049, P. R. China;* orcid.org/0000-0002-4883-5790; Email: chenshizhen@wipm.ac.cn

Xin Zhou − *State Key Laboratory of Magnetic Resonance Spectroscopy and Imaging, National Center for Magnetic Resonance in Wuhan, Wuhan Institute of Physics and Mathematics, Innovation Academy for Precision Measurement Science and Technology, Chinese Academy of Sciences-Wuhan National Laboratory for Optoelectronics, Huazhong University of Science and Technology, Wuhan 430071, P. R. China; University of Chinese Academy of Sciences, Beijing 100049, P. R. China; School of Biomedical Engineering, Hainan University, Haikou 570228, P. R. China;* orcid.org/0000-0002-5580-7907; Email: xinzhou@wipm.ac.cn

Authors

Mou Jiang − *State Key Laboratory of Magnetic Resonance Spectroscopy and Imaging, National Center for Magnetic Resonance in Wuhan, Wuhan Institute of Physics and Mathematics, Innovation Academy for Precision Measurement Science and Technology, Chinese Academy of Sciences-Wuhan National Laboratory for Optoelectronics, Huazhong University of Science and Technology, Wuhan 430071, P. R. China*

Yaping Yuan − *State Key Laboratory of Magnetic Resonance Spectroscopy and Imaging, National Center for Magnetic Resonance in Wuhan, Wuhan Institute of Physics and Mathematics, Innovation Academy for Precision Measurement Science and Technology, Chinese Academy of Sciences-Wuhan National Laboratory for Optoelectronics, Huazhong University of Science and Technology, Wuhan 430071, P. R. China; University of Chinese Academy of Sciences, Beijing 100049, P. R. China*

Yue Zhu − *State Key Laboratory of Magnetic Resonance Spectroscopy and Imaging, National Center for Magnetic Resonance in Wuhan, Wuhan Institute of Physics and Mathematics, Innovation Academy for Precision Measurement Science and Technology, Chinese Academy of Sciences-Wuhan National Laboratory for Optoelectronics, Huazhong University of Science and Technology, Wuhan 430071, P. R. China*

Zhihao Zhou − *State Key Laboratory of Magnetic Resonance Spectroscopy and Imaging, National Center for Magnetic Resonance in Wuhan, Wuhan Institute of Physics and Mathematics, Innovation Academy for Precision Measurement Science and Technology, Chinese Academy of Sciences-Wuhan National Laboratory for Optoelectronics, Huazhong University of Science and Technology, Wuhan 430071, P. R. China*

Tian Xia − *State Key Laboratory of Magnetic Resonance Spectroscopy and Imaging, National Center for Magnetic Resonance in Wuhan, Wuhan Institute of Physics and Mathematics, Innovation Academy for Precision Measurement Science and Technology, Chinese Academy of Sciences-Wuhan National Laboratory for Optoelectronics, Huazhong University of Science and Technology, Wuhan 430071, P. R. China*

Louis-S. Bouchard − *Department of Chemistry and Biochemistry, University of California, Los Angeles, California 90095, United States*

Complete contact information is available at: https://pubs.acs.org/10.1021/cbmi.5c00213

Author Contributions

The manuscript was collaboratively written with contributions from all authors, and all authors have approved the final version of the manuscript.

Notes

The authors declare no competing financial interest.

ACKNOWLEDGMENTS

This work was supported by the National Natural Science Foundation of China (82441015, 82127802, and 22525407), the CAS Youth Interdisciplinary Team (JCTD-2022-13), the Strategic Priority Research Program of the Chinese Academy of Sciences (XDC0170000), and the Hubei Provincial Natural Science Foundation of China (2023BAA021 and 2023BCB092).

REFERENCES

(1) Dienel, G. A. Brain Glucose Metabolism: Integration of Energetics with Function. *Physiol. Rev.* **2019**, *99* (1), 949−1045.

(2) Boado, R. J.; Black, K. L.; Pardridge, W. M. Gene expression of GLUT3 and GLUT1 glucose transporters in human brain tumors. *Brain Res. Mol. Brain Res.* **1994**, *27* (1), 51−57.

(3) Benner, T.; Heiland, S.; Erb, G.; Forsting, M.; Sartor, K. Accuracy of gamma-variate fits to concentration-time curves from dynamic susceptibility-contrast enhanced MRI: Influence of time resolution, maximal signal drop and signal-to-noise. *Magn. Reson. Imaging* **1997**, *15* (3), 307−317.

(4) Huang, J.; van Zijl, P. C. M.; Han, X.; Dong, C. M.; Cheng, G. W. Y.; Tse, K. H.; Knutsson, L.; Chen, L.; Lai, J. H. C.; Wu, E. X.; et al. Altered d-glucose in brain parenchyma and cerebrospinal fluid of early Alzheimer's disease detected by dynamic glucose-enhanced MRI. *Sci. Adv.* **2020**, *6* (20), No. eaba3884.

(5) Jadvar, H. PET of Glucose Metabolism and Cellular Proliferation in Prostate Cancer. *J. Nucl. Med.* **2016**, *57* (Suppl 3), 25S−29S.

(6) Mishkovsky, M.; Anderson, B.; Karlsson, M.; Lerche, M. H.; Sherry, A. D.; Gruetter, R.; Kovacs, Z.; Comment, A. Measuring glucose cerebral metabolism in the healthy mouse using hyperpolarized ^{13}C magnetic resonance. *Sci. Rep.* **2017**, *7* (1), No. 11719.

(7) Rich, L. J.; Bagga, P.; Wilson, N. E.; Schnall, M. D.; Detre, J. A.; Haris, M.; Reddy, R. ^{1}H magnetic resonance spectroscopy of ^{2}H-to-^{1}H exchange quantifies the dynamics of cellular metabolism in vivo. *Nat. Biomed. Eng.* **2020**, *4* (3), 335−342.

(8) Walker-Samuel, S.; Ramasawmy, R.; Torrealdea, F.; Rega, M.; Rajkumar, V.; Johnson, S. P.; Richardson, S.; Gonçalves, M.; Parkes, H. G.; Årstad, E.; et al. In vivo imaging of glucose uptake and metabolism in tumors. *Nat. Med.* **2013**, *19* (8), 1067−1072.

(9) Huang, J.; Lai, J. H. C.; Han, X.; Chen, Z.; Xiao, P.; Liu, Y.; Chen, L.; Xu, J.; Chan, K. W. Y. Sensitivity schemes for dynamic glucose-enhanced magnetic resonance imaging to detect glucose uptake and clearance in mouse brain at 3 T. *NMR Biomed.* **2022**, *35* (3), No. e4640.

(10) Serai, S. D. Basics of magnetic resonance imaging and quantitative parameters T_1, T_2, T_2*, T_{1rho} and diffusion-weighted imaging. *Pediatr. Radiol.* **2022**, *52* (2), 217−227.

(11) Jin, T.; Mehrens, H.; Hendrich, K. S.; Kim, S. G. Mapping brain glucose uptake with chemical exchange-sensitive spin-lock magnetic resonance imaging. *J. Cereb. Blood Flow Metab.* **2014**, *34* (8), 1402−1410.

(12) Ma, D.; Gulani, V.; Seiberlich, N.; Liu, K.; Sunshine, J. L.; Duerk, J. L.; Griswold, M. A. Magnetic resonance fingerprinting. *Nature* **2013**, *495* (7440), 187−192.

(13) Tippareddy, C.; Zhao, W.; Sunshine, J. L.; Griswold, M.; Ma, D.; Badve, C. Magnetic resonance fingerprinting: an overview. *Eur. J. Nucl. Med. Mol. Imaging* **2021**, *48* (13), 4189−4200.

(14) MacAskill, C. J.; Zhu, Y.; Wang, G.; Erokwu, B. O.; Dhakan, C. B.; Dupuis, A.; Schiemann, B. J.; Kavran, M.; Wu, C.; Schiemann, W. P.; et al. Dynamic contrast enhanced-magnetic resonance fingerprinting (DCE-MRF): A new quantitative MRI method to reliably assess tumor vascular perfusion. *Magn. Reson. Med.* **2025**, *94* (6), 2578−2592.

(15) Sharafi, A.; Zibetti, M. V. W.; Chang, G.; Cloos, M.; Regatte, R. R. MR fingerprinting for rapid simultaneous T_1, T_2, and $T_{1\rho}$ relaxation mapping of the human articular cartilage at 3T. *Magn. Reson. Med.* **2020**, *84* (5), 2636−2644.

(16) Ma, S.; Wang, N.; Fan, Z.; Kaisey, M.; Sicotte, N. L.; Christodoulou, A. G.; Li, D. Three-dimensional whole-brain simultaneous T_1, T_2, and $T_{1\rho}$ quantification using MR Multitasking: Method and initial clinical experience in tissue characterization of multiple sclerosis. *Magn. Reson. Med.* **2021**, *85* (4), 1938−1952.

(17) Sharafi, A.; Zibetti, M. V. W.; Chang, G.; Cloos, M.; Regatte, R. R. 3D magnetic resonance fingerprinting for rapid simultaneous T_1, T_2, and $T_{1\rho}$ volumetric mapping of human articular cartilage at 3 T. *NMR Biomed.* **2022**, *35* (12), No. e4800.

(18) Velasco, C.; Cruz, G.; Lavin, B.; Hua, A.; Fotaki, A.; Botnar, R. M.; Prieto, C. Simultaneous T_1, T_2, and $T_{1\rho}$ cardiac magnetic resonance fingerprinting for contrast agent-free myocardial tissue characterization. *Magn. Reson. Med.* **2022**, *87* (4), 1992−2002.

(19) Schuenke, P.; Paech, D.; Koehler, C.; Windschuh, J.; Bachert, P.; Ladd, M. E.; Schlemmer, H.-P.; Radbruch, A.; Zaiss, M. Fast and Quantitative $T1\rho$-weighted Dynamic Glucose Enhanced MRI. *Sci. Rep.* **2017**, *7* (1), No. 42093.

(20) Nezafat, R.; Stuber, M.; Ouwerkerk, R.; Gharib, A. M.; Desai, M. Y.; Pettigrew, R. I. B_1-insensitive T_2 preparation for improved coronary magnetic resonance angiography at 3 T. *Magn. Reson. Med.* **2006**, *55* (4), 858−864.

(21) Yang, Y.; Wang, C.; Liu, Y.; Chen, Z.; Liu, X.; Zheng, H.; Liang, D.; Zhu, Y. A robust adiabatic constant amplitude spin-lock preparation module for myocardial $T1\rho$ quantification at 3 T. *NMR Biomed.* **2023**, *36* (2), No. e4830.

(22) Hamilton, J. I.; Jiang, Y.; Ma, D.; Lo, W. C.; Gulani, V.; Griswold, M.; Seiberlich, N. Investigating and reducing the effects of confounding factors for robust T_1 and T_2 mapping with cardiac MR fingerprinting. *Magn. Reson. Imaging* **2018**, *53*, 40−51.

(23) Kim, D. H.; Adalsteinsson, E.; Spielman, D. M. Simple analytic variable density spiral design. *Magn. Reson. Med.* **2003**, *50* (1), 214−219.

(24) Wyatt, C. R.; Barbara, T. M.; Guimaraes, A. R. $T_{1\rho}$ magnetic resonance fingerprinting. *NMR Biomed.* **2020**, *33* (5), No. e4284.

(25) Zhao, B.; Haldar, J. P.; Liao, C.; Ma, D.; Jiang, Y.; Griswold, M. A.; Setsompop, K.; Wald, L. L. Optimal Experiment Design for Magnetic Resonance Fingerprinting: Cramer-Rao Bound Meets Spin Dynamics. *IEEE Trans. Med. Imaging* **2019**, *38* (3), 844−861.

(26) Liao, C.; Cao, X.; Iyer, S. S.; Schauman, S.; Zhou, Z.; Yan, X.; Chen, Q.; Li, Z.; Wang, N.; Gong, T.; et al. High-resolution myelin-water fraction and quantitative relaxation mapping using 3D ViSTa-MR fingerprinting. *Magn. Reson. Med.* **2024**, *91* (6), 2278−2293.

(27) Cao, X.; Liao, C.; Zhou, Z.; Zhong, Z.; Li, Z.; Dai, E.; Iyer, S. S.; Hannum, A. J.; Yurt, M.; Schauman, S.; et al. DTI-MR fingerprinting for rapid high-resolution whole-brain T_1, T_2, proton density, ADC, and fractional anisotropy mapping. *Magn. Reson. Med.* **2024**, *91* (3), 987−1001.

(28) Zhao, B.; Setsompop, K.; Adalsteinsson, E.; Gagoski, B.; Ye, H.; Ma, D.; Jiang, Y.; Grant, P. E.; Griswold, M. A.; Wald, L. L. Improved magnetic resonance fingerprinting reconstruction with low-rank and subspace modeling. *Magn. Reson. Med.* **2018**, *79* (2), 933−942.

(29) Uecker, M.; Lai, P.; Murphy, M. J.; Virtue, P.; Elad, M.; Pauly, J. M.; Vasanawala, S. S.; Lustig, M. ESPIRiT–an eigenvalue approach to autocalibrating parallel MRI: where SENSE meets GRAPPA. *Magn. Reson. Med.* **2014**, *71* (3), 990−1001.

(30) Beck, A.; Teboulle, M. A Fast Iterative Shrinkage-Thresholding Algorithm for Linear Inverse Problems. *SIAM J. Imaging Sci.* **2009**, *2* (1), 183−202.

(31) Kobayashi, Y.; Terada, Y. Diffusion-weighting Caused by Spoiler Gradients in the Fast Imaging with Steady-state Precession Sequence May Lead to Inaccurate T_2 Measurements in MR Fingerprinting. *Magn. Reson. Med. Sci.* **2019**, *18* (1), 96−104.

(32) Eleftheriou, A.; Ravotto, L.; Wyss, M. T.; Warnock, G.; Siebert, A.; Zaiss, M.; Weber, B. Simultaneous dynamic glucose-enhanced (DGE) MRI and fiber photometry measurements of glucose in the healthy mouse brain. *NeuroImage* **2023**, *265*, No. 119762.

(33) Weatherbee, A.; Popov, I.; Vitkin, A. Accurate viscosity measurements of flowing aqueous glucose solutions with suspended scatterers using a dynamic light scattering approach with optical coherence tomography. *J. Biomed. Opt.* **2017**, *22* (8), No. 087003.

(34) Bühler, I.; Walter, R.; Reinhart, W. H. Influence of D- and L-glucose on erythrocytes and blood viscosity. *Eur. J. Clin. Invest.* **2001**, *31* (1), 79−85.

(35) Dickie, B. R.; Jin, T.; Wang, P.; Hinz, R.; Harris, W.; Boutin, H.; Parker, G. J.; Parkes, L. M.; Matthews, J. C. Quantitative kinetic modelling and mapping of cerebral glucose transport and metabolism using glucoCESL MRI. *J. Cereb. Blood Flow Metab.* **2022**, *42* (11), 2066−2079.

(36) Tax, C. M. W.; Kleban, E.; Chamberland, M.; Baraković, M.; Rudrapatna, U.; Jones, D. K. Measuring compartmental T_2-orientational dependence in human brain white matter using a tiltable RF coil and diffusion-T_2 correlation MRI. *NeuroImage* **2021**, *236*, No. 117967.

(37) Akella, S. V.; Regatte, R. R.; Wheaton, A. J.; Borthakur, A.; Reddy, R. Reduction of residual dipolar interaction in cartilage by spin-lock technique. *Magn. Reson. Med.* **2004**, *52* (5), 1103−1109.

(38) Liao, C.; Bilgic, B.; Manhard, M. K.; Zhao, B.; Cao, X.; Zhong, J.; Wald, L. L.; Setsompop, K. 3D MR fingerprinting with accelerated stack-of-spirals and hybrid sliding-window and GRAPPA reconstruction. *NeuroImage* **2017**, *162*, 13−22.

(39) Mies, G. Measurement of in vivo glucose transport from blood to tissue of experimentally-induced glioma in rat brain. *J. Neuro-Oncol.* **1992**, *12* (1), 13−23.

(40) Liberti, M. V.; Locasale, J. W. The Warburg Effect: How Does it Benefit Cancer Cells? *Trends. Biochem. Sci.* **2016**, *41* (3), 211−218.

(41) Nasrallah, F. A.; Pagès, G.; Kuchel, P. W.; Golay, X.; Chuang, K. H. Imaging brain deoxyglucose uptake and metabolism by glucoCEST MRI. *J. Cereb. Blood Flow Metab.* **2013**, *33* (8), 1270−1278.

(42) Schuenke, P.; Koehler, C.; Korzowski, A.; Windschuh, J.; Bachert, P.; Ladd, M. E.; Mundiyanapurath, S.; Paech, D.; Bickelhaupt, S.; Bonekamp, D.; et al. Adiabatically prepared spin-lock approach for $T1\rho$-based dynamic glucose enhanced MRI at ultrahigh fields. *Magn. Reson. Med.* **2017**, *78* (1), 215−225.

(43) Jin, T.; Mehrens, H.; Wang, P.; Kim, S.-G. Glucose metabolism-weighted imaging with chemical exchange-sensitive MRI of 2-deoxyglucose (2DG) in brain: Sensitivity and biological sources. *NeuroImage* **2016**, *143*, 82−90.

(44) Zhang, D.; Li, J.; Wang, F.; Hu, J.; Wang, S.; Sun, Y. 2-Deoxy-D-glucose targeting of glucose metabolism in cancer cells as a potential therapy. *Cancer Lett.* **2014**, *355* (2), 176−183.

(45) Lund-Andersen, H. Transport of glucose from blood to brain. *Physiol. Rev.* **1979**, *59* (2), 305−352.

(46) Bleeker, E. J. W.; van Buchem, M. A.; Webb, A. G.; van Osch, M. J. Phase-based arterial input function measurements for dynamic susceptibility contrast MRI. *Magn. Reson. Med.* **2010**, *64* (2), 358−368.

(47) Spence, A. M.; Muzi, M.; Mankoff, D. A.; O'Sullivan, S. F.; Link, J. M.; Lewellen, T. K.; Lewellen, B.; Pham, P.; Minoshima, S.; Swanson, K.; et al. ^{18}F-FDG PET of Gliomas at Delayed Intervals: Improved Distinction Between Tumor and Normal Gray Matter. *J. Nucl. Med.* **2004**, *45* (10), 1653−1659.

(48) Jordan, S. P.; Hu, S.; Rozada, I.; McGivney, D. F.; Boyacioglu, R.; Jacob, D. C.; Huang, S.; Beverland, M.; Katzgraber, H. G.; Troyer, M.; et al. Automated design of pulse sequences for magnetic resonance fingerprinting using physics-inspired optimization. *Proc. Natl. Acad. Sci. U.S.A.* **2021**, *118* (40), No. e2020516118.